Topographically generated internal waves and boundary layer instabilities

Nancy Soontiens, Marek Stastna, and Michael L. Waite

Citation: Physics of Fluids **27**, 086602 (2015); doi: 10.1063/1.4929344
View online: http://dx.doi.org/10.1063/1.4929344
View Table of Contents: http://scitation.aip.org/content/aip/journal/pof2/27/8?ver=pdfcov
Published by the AIP Publishing

PHYSICS OF FLUIDS **27**, 086602 (2015)

Topographically generated internal waves and boundary layer instabilities

Nancy Soontiens,[1,a)] Marek Stastna,[2] and Michael L. Waite[2]
[1]*Department of Earth, Ocean, and Atmospheric Sciences, University of British Columbia, Vancouver, British Columbia V6T 1Z4, Canada*
[2]*Department of Applied Mathematics, University of Waterloo, 200 University Ave W, Waterloo, Ontario N2L 3G1, Canada*

(Received 6 January 2015; accepted 8 August 2015; published online 26 August 2015)

Flow over topography has been shown to generate finite amplitude internal waves upstream, over the topography and downstream. Such waves can interact with the viscous bottom boundary layer to produce vigorous instabilities. However, the strength and size of such instabilities depends on whether viscosity significantly modifies the wave generation process, which is usually treated using inviscid theory in the literature. In this work, we contrast cases in which boundary layer separation profoundly alters the wave generation process and cases for which the generated internal waves largely match inviscid theory. All results are generated using a numerical model that simulates stratified flow over topography. Several issues with using a wave-based Reynolds number to describe boundary layer properties are discussed by comparing simulations with modifications to the domain depth, background velocity, and viscosity. For hill-like topography, three-dimensional aspects of the instabilities are also discussed. Decreasing the Reynolds number by a factor of four (by increasing the viscosity), while leaving the primary two-dimensional instabilities largely unchanged, drastically affects their three-dimensionalization. Several cases at the laboratory scale with a depth of 1 m are examined in both two and three dimensions and a subset of the cases is scaled up to a field scale 10-m deep fluid while maintaining similar values for the background current and viscosity. At this scale, increasing the viscosity by an order of magnitude does not significantly change the wave properties but does alter the wave's interaction with the bottom boundary layer through the bottom shear stress. Finally, two subcritical cases for which disturbances are able to propagate upstream showcase a set of instabilities forming on the upstream slope of the elevated topography. The time scale over which these instabilities develop is related to but distinct from the advective time scale of the waves. At a non-dimensional time when instabilities have formed in the field scale case, no instabilities have yet formed in the lab scale case. [http://dx.doi.org/10.1063/1.4929344]

I. INTRODUCTION

Observations of the passage of topographically generated internal waves on the California shelf and the subsequent increase in sediment concentration well above the bottom has fostered the development of a branch of internal wave research focused on interactions with the bottom boundary layer.[1] Internal waves, which are ubiquitous features in the coastal oceans, are formed as a response to buoyancy forces in a stratified body of water. The passage of a stratified fluid over bottom topography causes vertical displacements that result in wave motion, the amplitude of which can reach tens of meters or larger.[2] The large wave-induced velocities can interact with the

a)nsoontie@eos.ubc.ca

viscous bottom boundary layer resulting in instabilities and vortex shedding under certain conditions.[3,4] Vortex shedding is of particular interest due to the production of high bottom stresses and increased potential for systematic sediment transport into the water column. The conditions that lead to instabilities that are efficient in transporting material out of the boundary layer are currently under investigation.

The waves reported by Bogucki *et al.*[1] were hypothesized to be resonantly generated by flow over topography and have been suggested to interact with the viscous bottom boundary layer to cause sediment resuspension through vortex shedding and high bottom shear stress. Bogucki and Redekopp[5] proposed a mechanism to explain the sediment resuspension behaviour and the effects of propagating internal solitary waves of elevation on the bottom. They observed that the wave-induced velocities beneath an internal solitary wave of elevation led to an adverse pressure gradient which, in turn, initiated a separation bubble within the boundary layer at the front of the wave. Using two-dimensional numerical simulations, they found that under certain conditions related to the wave amplitude and Reynolds number, this separation bubble could evolve into a global instability with large variations in both space and time. Other numerical studies of weakly nonlinear waves showed vortex shedding high into the water column.[4] Larger amplitude waves induce a stronger adverse pressure gradient and, as such, are more susceptible to vortex shedding. The vortex shedding and global instability produce strong bottom shear stresses which may enhance sediment resuspension.[6] This behaviour has also been examined numerically by Stastna and Lamb[7] who found that vortex shedding can occur when internal solitary waves of elevation travelled in the presence of a background current (as would be the case for resonantly generated waves) and that a trapped core was not necessary for vortex shedding to occur. Some observational and experimental studies suggest internal wave induced pumping of sediments high into the water column.[8,9]

Other computational and laboratory studies have worked to evaluate a critical wave amplitude and Reynolds number required for vortex shedding.[4,10] In particular, the laboratory experiments by Carr *et al.*,[10] which involved internal solitary waves of depression, found qualitative agreement in the behaviour of vortex shedding with the two-dimensional numerical results of Diamessis and Redekopp.[4] However, several quantitative discrepancies were also found. For example, the critical wave amplitude required for the onset of global instability found in the laboratory experiments was roughly half that found by the numerical simulations. This is perhaps due to the three-dimensional effects that are present in the laboratory experiments but not in the numerical studies. Another possible reason for the discrepancy is that the weakly nonlinear representation of large waves used by Diamessis and Redekopp[4] may lead to an overestimate in the prevalence of vortex shedding.[7] Under certain stratification conditions, KdV or first order weakly nonlinear theory is known to overestimate wave speeds (and wave-induced currents) and underestimate wave widths for large waves, or those beyond the formal range of validity for the theory. In fact, the absence of vortex shedding in the laboratory experiments of internal solitary waves of elevation under parameter regimes where shedding was observed in the numerical simulations of Diamessis and Redekopp[4] indicates that care should be taken when studying this phenomenon numerically. Particularly, it is important for simulations to include realistic nonlinear internal waves, either with the Dubreil-Jacotin-Long (DJL) equation[11] or direct simulation. Further, reports of stability regimes in two-dimensional simulations of fully nonlinear waves[12] and weakly nonlinear waves[4] both show inconsistencies with laboratory experiments[10] suggesting that three-dimensional effects are very important.

The mechanisms that lead to the generation of these large internal waves have been under investigation for some time, with stratified flow over topography a primary example.[13–15] One particular case is the resonant generation of internal waves.[14,16] Some of these large waves are found in the lee of the topography, others advance slowly upstream and a third class remains trapped over the topography. While the majority of past theoretical and numerical work has considered the inviscid situation, it is likely that all three classes of waves may attain amplitudes large enough to induce near bed instability. This has been suggested by multiple authors in field, experimental, and numerical work.[1,7,12,17] Recent numerical work has confirmed that sediment resuspension occurs in a coupled hydrodynamic-sediment model.[6] More broadly, a wide variety of field studies have pointed to a link between increased near-bed sediment concentrations and shoaling internal waves

on a slope.[18–22] Quaresma *et al.*[8] have offered clear evidence of nonlinear internal waves influencing sediment resuspension over the northern shelves of Portugal. Bottom shear stress calculations suggested that the strongest nonlinear internal waves were capable of suspending sediment. The laboratory experiments of Aghsaee and Boegman[9] show that the vertical velocities induced by bursting motions in the boundary layer are important factors in sediment resuspension.

While the inviscid situation is clear, with large waves generated efficiently by topography when the Froude number (the ratio between the background velocity and the linear long wave internal wave speed) is near critical (i.e., $Fr \approx 1$), the viscous situation is somewhat more complex. Historically, a Reynolds number based on the channel depth and the linear long wave speed has been quoted when describing flow conditions.[4,10] The dependence on the linear long wave speed is *a priori* incorrect since a small wave with weak currents would have the same Reynolds number as a large wave with strong currents. If one focuses on large waves, the typical horizontal current magnitude will be well estimated by the linear long wave speed (though lower than the actual wave speed for non-breaking waves). The appropriateness of the channel depth remains under discussion. Recently, Aghsaee *et al.*[12] have proposed an alternate Reynolds number based on the momentum thickness for diagnosing and predicting vortex shedding behaviour. This alternate formulation has the advantage that it does not depend on the stratification profile.

The present study uses numerical simulations to investigate the interaction between internal waves generated by flow over isolated topography and the viscous boundary layer. In accord with the current literature on internal waves and boundary layer interactions, our focus is on lab-scale flows of 1 m depth, along with velocity and length scales typical of laboratory experiments.[10] However, we do consider a few field-scale cases with depth increased to 10 m with similar values for the viscosity and background current. At both laboratory and field scales, the dependence of the results on viscosity is considered by changing the value of the viscosity. The intent is to consider situations that would be equivalent in inviscid theory as far as wave generation is concerned, but for which boundary layer effects occupy a different fraction of the water column. It is computationally expensive to model these flows at field scales since both the internal waves and boundary layer must be well-resolved. As such, prior numerical studies have primarily focused on two-dimensional simulations; however, three-dimensional effects may be important in the evolution of instabilities associated with separation regions.[23] Some work has been completed on the three-dimensionalization of internal waves shoaling over isolated topography and the generation of near-bed instabilities.[6] This work also included a sediment resuspension model and found that three-dimensional effects can influence the deposition of suspended sediment. The three-dimensional characteristics of boundary layer instabilities that form due to internal solitary wave interaction with isolated topography has also been investigated[24] finding that separation-induced instabilities exhibit strong three-dimensionalization. Further, recent numerical studies of shoaling internal waves suggest differences in the amount of dissipation and mixing in two versus three dimensions.[25] It is therefore important to examine the three-dimensional nature of boundary layer instabilities in more detail.

This study aims to understand the three-dimensional aspects of bottom boundary layer instabilities and the role that viscosity plays in their evolution. In all simulations, a fluid with a pycnocline stratification initially at rest is gently accelerated from left to right until the background current reaches a pre-determined constant value. The stratified fluid interacts with a bottom topography to generate internal waves over and in the lee of the topography and the currents induced by these waves interact with the viscous bottom boundary layer to produce bottom boundary layer instabilities. Primarily, elevated topography with the pycnocline relatively close to the bottom boundary in supercritical flows for which no upstream propagating modes exist is considered. Many lakes are stratified with a pycnocline above the mid-depth but there are some examples of lakes with bottom layer stratifications.[26] Two cases with depression topography and a pycnocline stratification above the mid-depth are also presented. Previous work using a steady inviscid theory has shown that very large amplitude trapped internal waves exist over both elevated and depression topography in flow conditions where no upstream propagating modes exist.[15] These large wave states have motivated the cases considered in this study which investigates wave formation in the presence of a viscous boundary layer. Simulations in both two and three dimensions are considered.

The article is organized as follows: First, a description of the methods used in this study is provided in Section II. This includes an overview of the numerical model employed, the relevant non-dimensional parameters, some calculations for useful diagnostics, and a description of the domain and flow fields. Next, Section III introduces the results which examine boundary layer instabilities downstream of flow over elevated topography, as well as a simple depression topography case. Finally, a discussion which links this work to the relevant literature and outlines avenues for future research is provided in Section IV.

II. METHODOLOGY

Numerical simulations of a stratified fluid flowing over elevation and depression topography are discussed. The fluid density is initially given as a single pycnocline stratification and the upstream background current is set to a constant value U_0 away from the boundaries. In most cases, the flow is supercritical so that no upstream propagating modes exist. This condition is satisfied when $U_0 > c_j$, where c_j is the conjugate flow speed.[27,28] One subcritical case for which upstream propagating modes are permitted is also considered. In this case, the background flow satisfies $c_{lw} < U_0 < c_j$, where c_{lw} is the linear long wave speed.

The undisturbed density profile is given by

$$\rho(z) = 1 - \Delta\rho \tanh\left(\frac{z - z_0}{d_0}\right).$$

This density profile has been normalized by a constant reference value ρ_0.[29] A reference density typical of water $\rho_0 = 1000$ kg m^{-3} is used in calculations of the bottom shear stress. Other density parameters are $z_0 = 0.3H$, $d_0 = 0.1H$, and $\Delta\rho = 0.02$, where H is the depth of the domain. A summary of the simulation parameters is provided in Tables I and II.

The topography profile is given by

$$h(x) = \frac{h_0}{2}\left(\tanh\left(\frac{x + x_L/2}{\delta_x}\right) - \tanh\left(\frac{x - x_L/2}{\delta_x}\right)\right),$$

where h_0 is the topographic amplitude, x_L defines the width of the topography, and δ_x is a parameter that determines the slope. The elevated topography uses $h_0 = 0.1H$, $x_L = 3H$, and $\delta_x = 0.5H$ resulting in a flat-topped hill with gradual slopes. One case with depression topography is also presented with $h_0 = -0.1H$ and the location of the pycnocline center moved to $z_0 = 0.7H$.

Model runs are characterized by the Reynolds number, defined as

$$Re = \frac{U_0 H}{\nu},$$

where ν is the kinematic viscosity. There are several other definitions of the Reynolds number in the literature pertaining to boundary layer instabilities and internal waves.[4,12] In some literature, vortex shedding has been characterized with respect to a Reynolds number based on the linear long wave speed, c_{lw}.[4,10] This wave speed based Reynolds number is defined as

$$Re_w = \frac{c_{lw} H}{\nu}$$

TABLE I. Domain and stratification parameters for lab scale and field scale simulations. L_x (m), L_y (m), and H (m) are the length of the domain in the x, y, and z directions, respectively. Δx (m) and Δy (m) are the horizontal grid spacings and N_z is the number of grid points in the vertical. The maximum and minimum vertical grid spacing Δz (m) is also presented. The velocity scales, c_j, and c_{lw} have units m s^{-1}. Finally, T is the time over which the fluid was accelerated from rest.

	$L_x \times L_y \times H$	$\Delta x \times \Delta y \times N_z$	Min/max Δz	$\Delta\rho$	c_j	c_{lw}	T
Lab scale	$14 \times 0.1 \times 1$	$0.005 \times 0.002 \times 192$	$6 \times 10^{-5}/0.008$	0.02	0.28	0.25	$1.8t^*$
Field scale	$150 \times 0.1 \times 10$	$0.006 \times 0.001 \times 768$	$4 \times 10^{-5}/0.02$	0.005	0.44	0.4	$0.88t^*$

TABLE II. Summary of simulation parameters. ν is the viscosity ($m^2\ s^{-1}$) and U_0 is the background current ($m\ s^{-1}$). The two-dimensional simulations (labelled 2D) span the x and z directions only. Values for c_j and c_{lw} are listed in Table I.

Lab scale	Simulation	Re	Re_w	U_0	ν
Valley	2DLVa	3.5×10^5	2.5×10^5	$1.25c_j$	10^{-6}
	2DLVb	3.1×10^5	2.5×10^5	$1.11c_j$	10^{-6}
Hill	2DL1	3.5×10^5	2.5×10^5	$1.25c_j$	10^{-6}
	2DL2	2.5×10^6	2.5×10^6	$1.25c_j$	10^{-7}
	3DL1	3.5×10^5	2.5×10^5	$1.25c_j$	10^{-6}
	3DL2	1.75×10^5	1.25×10^5	$1.25c_j$	2×10^{-6}
	3DL3	8.75×10^4	6.25×10^4	$1.25c_j$	4×10^{-6}
	2DLS	2.63×10^5	2.5×10^5	$1.05c_{lw}$	10^{-6}
Field scale	Simulation	Re	Re_w	U_0	ν
Hill	2DF1	5.5×10^6	4×10^6	$1.25c_j$	10^{-6}
	2DF2	5.5×10^5	4×10^5	$1.25c_j$	10^{-5}
	3DF1	5.5×10^6	4×10^6	$1.25c_j$	10^{-6}
	2DFS	4.2×10^6	4×10^6	$1.05c_{lw}$	10^{-6}

and ultimately depends on the density stratification through c_{lw}. This definition is problematic because given a certain stratification, a large amplitude wave with large wave-induced velocities would yield the same Reynolds number as a small wave with small wave-induced velocities. An alternate definition based on the momentum thickness at the separation point has also been used in the literature.[12] Since the viscosity is the main parameter of interest in these simulations, the Reynolds number defined by Re seems to be a natural choice for the current discussion. We calculate Re_w for comparison with the other studies mentioned.

The simulations are performed using a pseudospectral model that integrates the Navier-Stokes equations of motion for an incompressible fluid under the Boussinesq approximation.[29] The numerical model includes several useful features such as grid mapping for topography, free slip or no slip boundary conditions in the vertical, the ability to simulate two- and three-dimensional flows, and adaptive time-stepping, all in a scalable, parallelized framework. The configuration employed here consists of periodic horizontal boundary conditions and a Chebyshev discretization in the vertical with no slip boundary conditions. The spectral method allows for high accuracy with only moderate grid sizes, and the Chebyshev grid naturally clusters points in the boundary layer where instabilities develop. The numerical model employs a filtering technique to eliminate aliasing errors introduced by the spectral representation of the Navier-Stokes equations.[29] The simulations are terminated prior to the onset of significant turbulent break down where the smallest turbulent eddy scales become smaller than the grid spacing, and also before wraparound effects associated with the periodic horizontal boundary conditions occur.

The simulation is commenced by accelerating a fluid at rest over a period T (defined in Table I) up to a constant background speed U_0. In the three-dimensional simulations, the flow is first integrated in two dimensions and the two-dimensional flow fields are used to initialize a three-dimensional simulation with a small amount of white noise with amplitude less than 0.01 to perturb the flow and trip any spanwise instabilities that develop. This process allows for three-dimensional runs in a more time efficient manner, since three-dimensional simulations are very expensive computationally. The time step is mainly restricted by the small grid spacing imposed by Chebyshev grid, even when the flow is primarily two-dimensional at the beginning of the simulation, so including the third dimension at the start of the simulation adds no extra value. Tables I and II outline the relevant physical parameters for the lab scale and field scale simulations. Note that all simulations except 2DLVb, 2DLS, and 2DFS use a background speed $U_0 = 1.25c_j$ and both of the subcritical lab scale (2DLS) and field scale (2DFS) simulations use $U_0 = 1.05c_{lw}$. The results are discussed in terms of non-dimensional values with distances scaled by the domain

height H, velocities scaled by the conjugate flow speed c_j, and times scaled by the advective time scale $t^* = H/c_j$. The simulations were performed on the GPC supercomputer at the SciNet HPC Consortium.[30]

The physical domain for both the lab scale and field scale simulations are outlined in Table I as well as the details of the numerical discretization. In each simulation, the grid is stretched vertically which results in higher resolution near the upper and lower boundaries leaving the boundary layer instabilities very well resolved. For example, late into the lab-scale simulations at $t \approx 20t^*$ there are approximately 30 grid points across the 0.04 m thick boundary layer. In the three-dimensional simulations, the streamwise and spanwise grid spacings were chosen to be about the same order of magnitude, however, Δy is slightly smaller than Δx.

Parameter choices for each simulation are outlined in Table II. In general, the parameters that are varied between simulations are the background current U_0 and the viscosity ν which lead to changes in the Reynolds number. Modifying the size of the domain also changes the Reynolds number through the vertical length scale H. The purpose of increasing the vertical length scale is to compare situations that would be equivalent in inviscid theory but for which boundary layer effects occupy a different fraction of the water column.

An important factor when considering how internal waves interact with the bottom boundary is the bottom shear stress. In the case of two-dimensional flow over a flat bottom, the expression for the bottom shear stress is

$$\tau = \mu \frac{du}{dz}\bigg|_{z=0}, \tag{1}$$

where $\mu = \nu/\rho_0$. Over a sloping boundary, the expression is slightly more complicated but can be derived from Cauchy's stress theorem[31] which relates the stress vector to the Cauchy stress tensor, τ_{ij},

$$t_i = \tau_{ij} n_j, \tag{2}$$

where t_i is the stress vector in a plane with unit normal vector n_i. The bottom shear stress is the tangential component of the stress vector evaluated at the surface $z = h(x)$. In the case of an incompressible fluid this works out to

$$\tau = \frac{2\mu h'(x)\left(w_z - u_x\right) + \mu\left(1 - h'(x)^2\right)\left(u_z + w_x\right)}{1 + h'(x)^2}\bigg|_{z=h(x)}, \tag{3}$$

where the prime denotes differentiation with respect to x and the underscores represent partial differentiation. After applying no slip and no normal flow boundary conditions, this expression further simplifies to

$$\tau = \frac{\mu\left(h'(x) w_z + u_z\right)}{1 + h'(x)^2}\bigg|_{z=h(x)}. \tag{4}$$

To analyse the three-dimensional characteristics of the flow field, we make use of several diagnostics based on the kinetic energy per unit mass,

$$KE = \frac{1}{2}\left(u^2 + v^2 + w^2\right). \tag{5}$$

First, the kinetic energy averaged in the spanwise direction scaled by the maximum kinetic energy reveals parts of the flow with strong two-dimensional energy, and how the mean kinetic energy profile relates to the pointwise maximum. Second, we calculate the standard deviation of the kinetic energy in the spanwise direction scaled by the maximum kinetic energy. This diagnostic reveals how three-dimensional the flow is and identifies areas of high three-dimensionality. Higher departures from the mean (or higher standard deviations) indicate that the flow is more three-dimensional.

III. RESULTS

This study is focused on the formation of boundary layer instabilities and flow over topography. First, a general overview of the internal wave generation and boundary layer interaction is included

for both elevation and depression topographies at lab scales (14 m by 1 m). Next, a discussion of the three-dimensionalization of these instabilities in cases of elevation topography is provided in Section III A, followed by some examples of how these results carry over to larger scales (150 m by 10 m) in Section III B. Finally, several subcritical cases for which waves can propagate upstream are examined in Section III C.

First, a comparison between flow over hill and valley topography in two dimensions is presented in Figure 1 as a general overview of the types of waves and instabilities generated in these scenarios. As described by Soontiens *et al.*,[15] large trapped waves over topography can be expected in inviscid, supercritical flow over depression topography when the pycnocline is centered above the mid-depth and in flow over elevated topography when the pycnocline is centered below the mid-depth. These large-amplitude cases have motivated simulations 2DL1 and 2DLVa which examine flow over elevated and depression topography, respectively. The pycnocline is centered at $z_0 = 0.3H$ in the elevation case and $z_0 = 0.7H$ in the depression case. Both of these simulations have the same Reynolds number as outlined in Table II. A third case, 2DLVb, with a lower background speed, and hence, lower Reynolds number, but larger amplitude inviscid solution is also considered.

The elevation case exhibits a large wave over the topography followed by a depression wave in the topographic lee depicted in Figure 1. The large velocities induced by this feature interact with the viscous bottom boundary layer to produce the boundary layer instabilities in the topographic lee observed in panels (a)–(c). At the earliest time $t = 5.6t^*$ in panel (a), the instabilities are just beginning to form and are manifested as small oscillations within the boundary layer around $x = 3$.

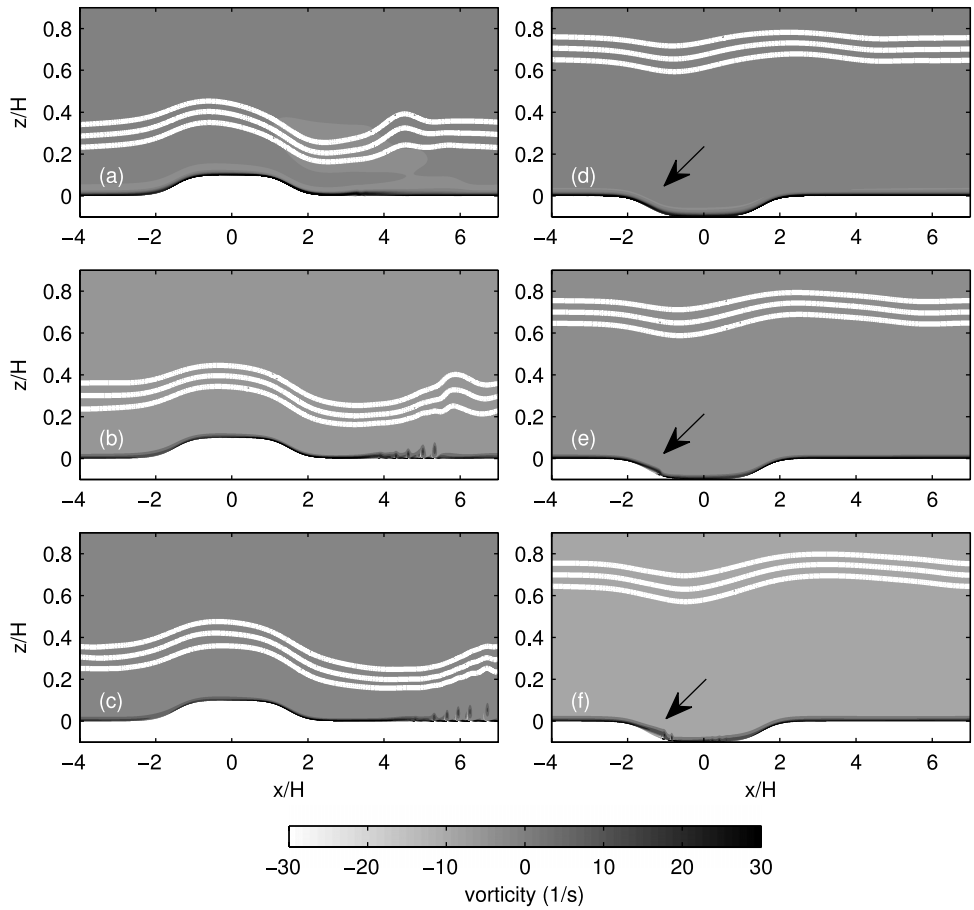

FIG. 1. Comparison of evolution for hill (2DL1) and valley (2DLVa) lab scale simulations. Shaded contours of the vorticity are overlaid with three white isopycnals. The times displayed are $t = 5.6t^*$, $t = 7.8t^*$, and $t = 10t^*$ from top to bottom. Arrows aid in visualization of the instabilities in the depression case.

Later, the vortical shape of the instabilities is more apparent and their vertical extent reaches high enough to interact with the pycnocline as observed in the small undulations in the white isopycnals.

In the case of propagating internal waves, previous research has indicated that boundary layer instabilities like the ones shown in Figures 1(a)-1(c) form due to the adverse pressure gradient induced by the internal waves.[4,5] These studies have focused on internal solitary waves, however, the depression wave in the topographic lee is not an exact solitary wave since its shape changes slowly over time. Nonetheless, the large wave-induced velocities beneath this feature produce a convergence zone at the front and a separation bubble within the boundary layer in a similar manner as the adverse pressure gradient of internal solitary waves. This type of instability generation mechanism has been discussed by Stastna and Lamb[7] for resonantly generated internal waves over topography. Although not shown here, instabilities also begin to form on the upstream slope of the topography after longer integration times at $t \approx 17.5t^*$.

The depression case in panels (d)–(f) exhibits instabilities that form in a different location relative to the topography. A small wave of depression has formed over the topography along with a rather small wave of elevation in the topographic lee. In this case, boundary layer instabilities form on the leading slope of the topographic depression, most apparent at the latest time in panel (f) at $t = 10t^*$. These instabilities remain confined to the boundary layer and are formed due to separation over the topographic slope. The small wave in the topographic lee for this depression case is not associated with the strong wave-induced currents required to excite bottom boundary layer instabilities downstream of the topography. By contrast, the elevation case exhibits a large lee wave with very strong currents and subsequent instability generation. The same physical mechanism is responsible for the development of these instabilities, that is, an adverse pressure gradient leads to separation and instability generation.

A schematic diagram in Figure 2 provides a simple illustration of the development of the separation bubble in each case. In the elevation case, panel (a), a large lee wave produces a region of accelerated flow in the topographic lee resulting in convergence at the downstream edge of the accelerated region. At this point, the fluid is decelerating and the resulting adverse pressure gradient leads to a separation bubble and subsequent instabilities. The stratification plays a role in the strength of the adverse pressure gradient. A large lee wave would lead to a stronger deceleration and hence stronger adverse pressure gradient. The size of the lee wave is influenced by the depth of the pycnocline and the strength of background current.

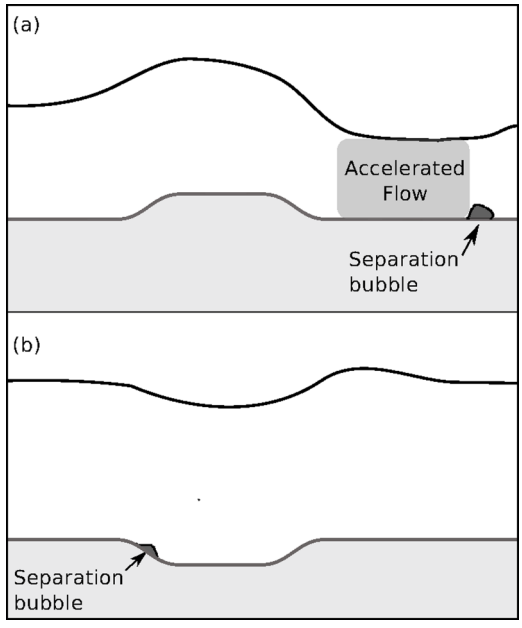

FIG. 2. Schematic diagram demonstrating the development of the separation bubble in the (a) elevation case and (b) depression case.

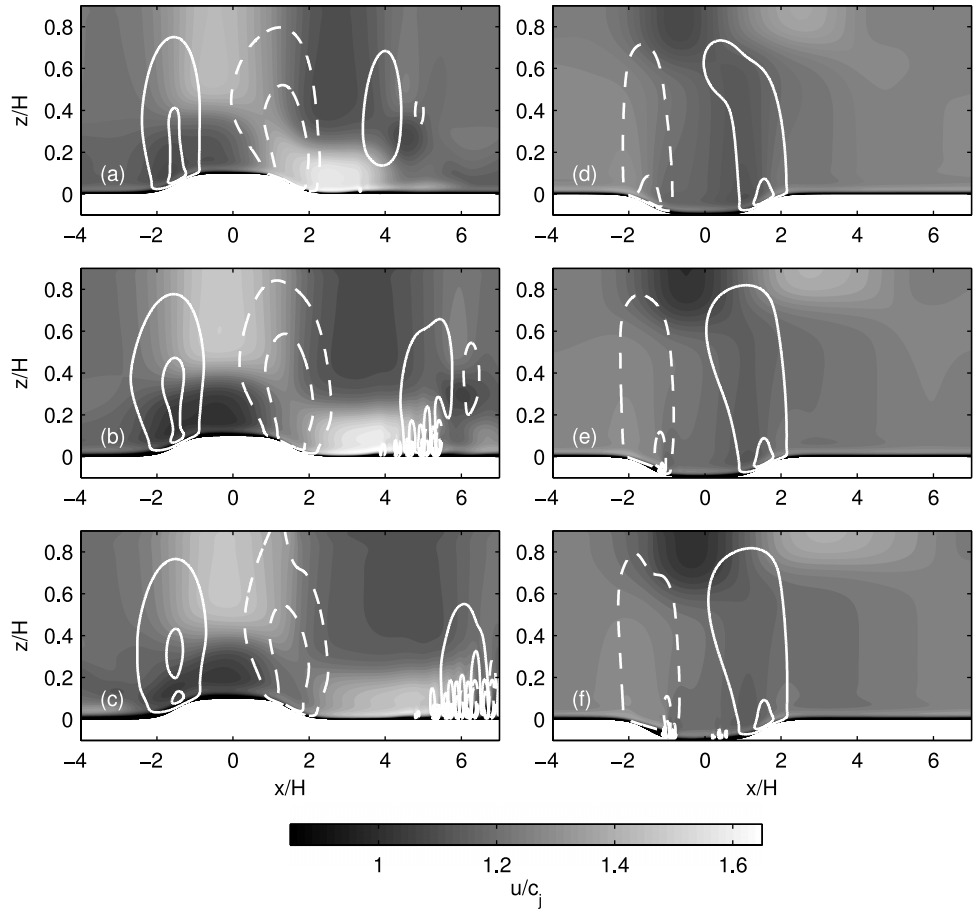

FIG. 3. Evolution of velocity fields for hill (2DL1) and valley (2DLVa) lab scale simulations. Shaded contours of the horizontal velocity overlaid with white contours of vertical velocity. Contours for $\pm[0.036\ 0.089\ 0.18]c_j$ are displayed. Solid lines are positive, dashed negative. The times are the same as those displayed in Figure 1.

In the depression case, panel (b), the instabilities develop on the upstream slope due to separation from the topography. As the pycnocline dips slightly downwards, the fluid accelerates along the slope and then decelerates near the bottom where the flow separates as a result of the adverse pressure gradient.

The velocity fields displayed in Figure 3 further demonstrate the evolution of these instabilities. The velocity fields are scaled by the conjugate flow speed c_j listed in Table I. Since both stratifications have the same conjugate flow speed, the magnitude of the streamwise velocity is easily compared through the intensity of the shaded contours. The elevation case produces much higher streamwise velocities and exhibits a complicated interaction with the bottom boundary layer that extends high into the water column. On the other hand, the depression case exhibits more moderate streamwise velocities and the instabilities remain confined to the bottom boundary and do not interact with the overlying wave of depression. Further, it is seen clearly that the instabilities form in decelerating regions for both the elevation and depression cases. Note that the distribution of the streamwise velocity is much different between the two cases. For the elevation case, a large trapped wave over the topography results in reduced velocities beneath the pycnocline that extends over much of topography at later times (panel (c)). In the depression case, no large trapped wave has formed and at later times (panel (f)), the streamwise velocity away from the boundary layer but below the pycnocline is roughly antisymmetric across the topographic midpoint.

An additional comparison is carried out in Figure 4 where we have plotted the departure of the bottom shear stress from its upstream value over time for each case. In the elevation case, high

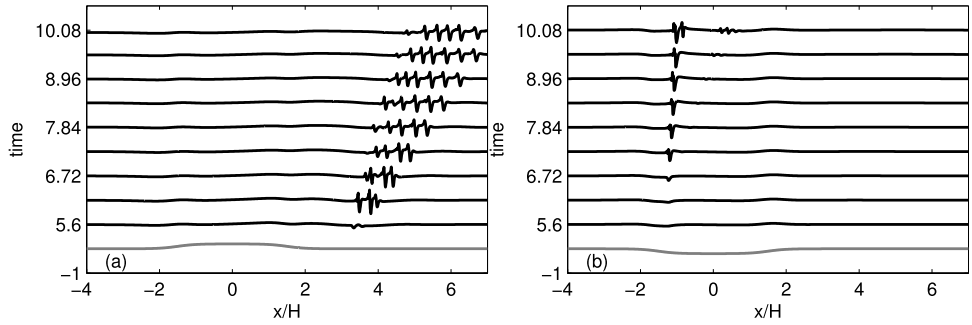

FIG. 4. The departure of bottom shear stress from its upstream values at several times for cases (a) 2DL1 and (b) 2DLVa. The vertical axis indicates the non-dimensional time (scaled by t^*) of each stress calculation and the horizontal axis is the streamwise position. The gray curve represents the topography. The maximum stress reached up to 13 times the upstream value in 2DL1 and 15 times the upstream value in 2DLVa.

values of shear stress span a large distance downstream of the topography. The depression case exhibits large stress values along the upstream topographic slope and a set of instabilities beginning to form in the center of the depression. At later times, these instabilities grow and travel downstream. Note that the onset of large stress in the depression case occurs later into the simulation.

These simulations were motivated by large amplitude solutions to a steady state inviscid problem.[15] Next, we examine how the viscous boundary layer modifies trapped wave formation. In the case of depression topography, the presence of the viscous boundary layer can greatly alter the wave generation process, as demonstrated in Figure 5 where we plot the density field from inviscid steady theory and time-dependent simulations using the parameters in simulations 2DLVa and 2DLVb. The inviscid results are solutions to the DJL equation, a single nonlinear partial differential equation for the isopycnal displacement that is equivalent to the steady Euler equations of motion. The solution procedure is described by Soontiens *et al.*[15] who found that very large trapped waves over depression topography can exist if the background speed U_0 is close to the conjugate flow speed c_j. Large waves over elevation topography also exist but do not reach the same amplitudes. For the parameters given in 2DLVa, the inviscid theory in panel (a) produces a wave of moderate

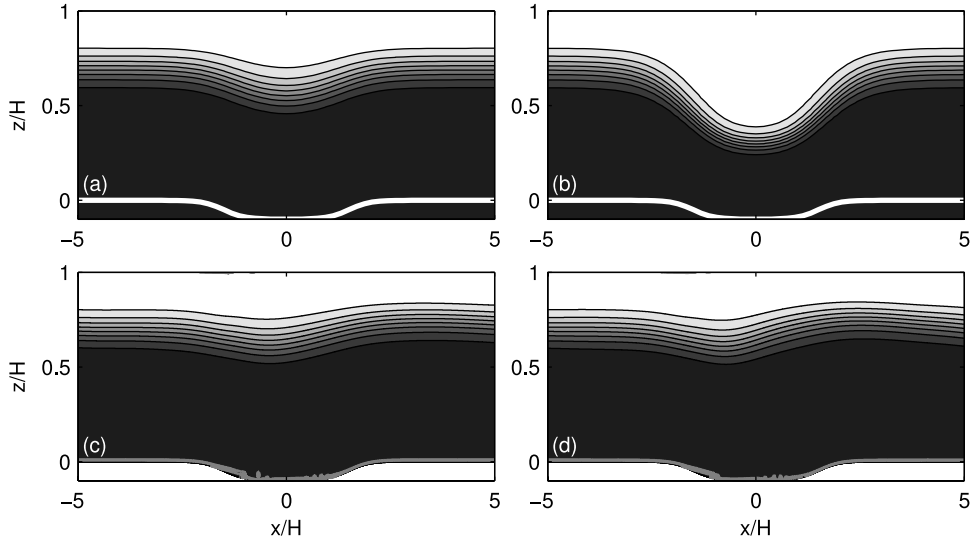

FIG. 5. Density field from inviscid theory (top) compared with density field from simulations (bottom) at $t = 10.6t^*$. Parameters from simulation 2DLVa were used to generate the inviscid plot in (a) and simulation plot in (c). 2DLVb parameters result in the inviscid plot (b) and simulation (d). The simulation plots also include gray vorticity contours in the bottom boundary layer to showcase the instabilities.

amplitude slightly larger than the topographic amplitude. Under viscous conditions, at the time plotted ($t = 10.6t^*$), the simulation in panel (c) showcases a wave that is slightly smaller than that expected based on inviscid theory, although a steady state has not yet been obtained. By reducing the background speed slightly to $U_0 = 1.1c_j$, the inviscid theory in panel (b) predicts a very large wave trapped over topography that is not reproduced by the viscous simulations in (d). The separation and boundary layer instabilities alter the wave generation process in this case. Outside of the boundary layer and away from the wave disturbances, the horizontal velocity in both the inviscid solution and the viscous simulation take on similar values ($1.1c_j$ and $1.12c_j$, respectively). Similarly, in the more supercritical case (panels (a) and (c)), the far-field horizontal velocity values in the inviscid solution and viscous simulation are $1.25c_j$ and $1.28c_j$, respectively. The waves in each of the simulations look very similar whereas the inviscid solutions are quite different. By contrast, supercritical inviscid waves over elevated topography predicted by steady theory are similar to those produced in the numerical simulations (not shown). It is likely that the separation on the slope of the depression topography modifies the flow enough to prevent the formation of a large trapped wave of depression. In the elevation case, the separation occurs downstream of the topography, hence, the trapped wave is unmodified. These results underline the danger of extrapolating too much from inviscid simulations.

A. Three-dimensionalization

Many numerical studies on internal waves and boundary layer interaction have been two-dimensional, due to the high computational expense of resolving both the internal wave and the bottom boundary layer.[4,7,12] However, the often vigorous motions associated with the destabilization of a separation bubble in the viscous boundary layer are undoubtedly subject to three-dimensionalization in a physical flow environment.[23] To investigate the potential for three-dimensionalization and dependence on viscosity, we have performed several three-dimensional simulations. The three-dimensional simulations are started at time $t = 5.04t^*$ and the velocity fields are perturbed with white noise of amplitude $0.0001c_j$. The spanwise extent of the domain is 10 cm. With these choices, three-dimensional effects become apparent around $t = 6.44t^*$.

Three-dimensional characteristics are displayed in Figure 6 where we have plotted the results for simulation 3DL1 with $Re = 3.5 \times 10^5$ at time $t = 6.44t^*$. First, in Figure 6(a) the mean kinetic energy shows the signature of the internal wave overlying the topography as well as the downstream instabilities in the topographic lee. It is clear that the maximum kinetic energies occur in the instabilities. This region is outlined by the dashed white rectangle. These instabilities induce

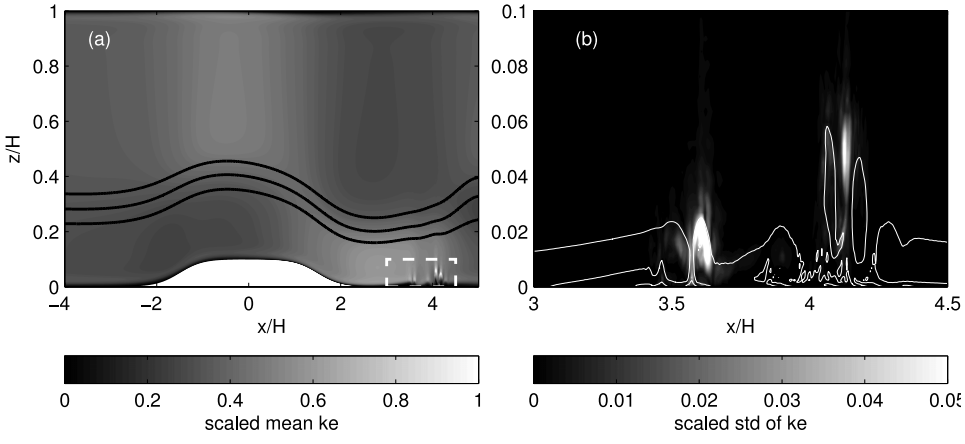

FIG. 6. Results for simulation 3DL1 at time $t = 6.44t^*$. (a) The kinetic energy averaged across the spanwise direction scaled by the maximum of the kinetic energy. Three black density contours are included. The white-dashed rectangle indicates the viewing area of panel (b). (b) The spanwise standard deviation of the kinetic energy scaled by the maximum kinetic energy. The white contours show the spanwise vorticity averaged across the spanwise direction. The contour level is 15 s^{-1}. The maximum pointwise kinetic energy at this time was 0.17 $m^2\ s^{-2}$.

large fluctuations in the velocity fields, resulting in the high values of kinetic energy. The spanwise standard deviation of the kinetic energy in this region is displayed in Figure 6(b) where the instabilities induce significant three-dimensional structure with departures greater than 10% of the maximum kinetic energy. Two vortical structures are observed in this plot at $x = 3.6$ and $x = 4.1$. The first instance contains the largest departures from the mean and the three-dimensional structure is concentrated at the center of the vortex. The second instance extends higher into the water column and the largest departures from the mean occur along a longer vertical filament. This plot indicates that significant three-dimensional motions can occur close to the boundary layer and higher into the water column as the instabilities separate from the boundary. A three-dimensional simulation over depression topography also demonstrated significant three-dimensionalization of the boundary layer instabilities, although these instabilities remained confined to the boundary layer (not shown).

Further, we have examined the spanwise variation in the bottom shear stress at this time, as well as the spanwise shear stress, μv_z, in Figure 7. The spanwise shear stress (panel (b)) shows a significant amount of structure in the spanwise dimension between $x = 3.55$ and $x = 3.7$. While some spanwise variation is also visible in the bottom shear stress (panel (a)), it is not as significant as the variation in the spanwise shear stress. At this time, the absolute maximum of the bottom shear stress was about an order of magnitude larger than the absolute maximum of spanwise shear stress.

Two additional cases are considered from simulation 3DL2 with $Re = 1.75 \times 10^5$ and simulation 3DL3 with $Re = 8.75 \times 10^4$, i.e., the viscosity has been increased by a factor of two in each subsequent case. The results are displayed in Figures 8 and 9, respectively. In the 3DL2 simulation (Figure 8), a similar scenario to that which was observed in the 3DL1 simulation occurs. The largest values of the mean kinetic energy are located in the downstream boundary layer instabilities displayed in Figure 8(a). Additionally, the two vortices in Figure 8(b) exhibit a similar structure to that seen previously, however, the departures from the mean are smaller than the higher Reynolds number case (the maximum kinetic energies are very similar in both cases). The increased viscosity dampens the motion in the boundary layer, resulting in an overall decrease in three-dimensional structure.

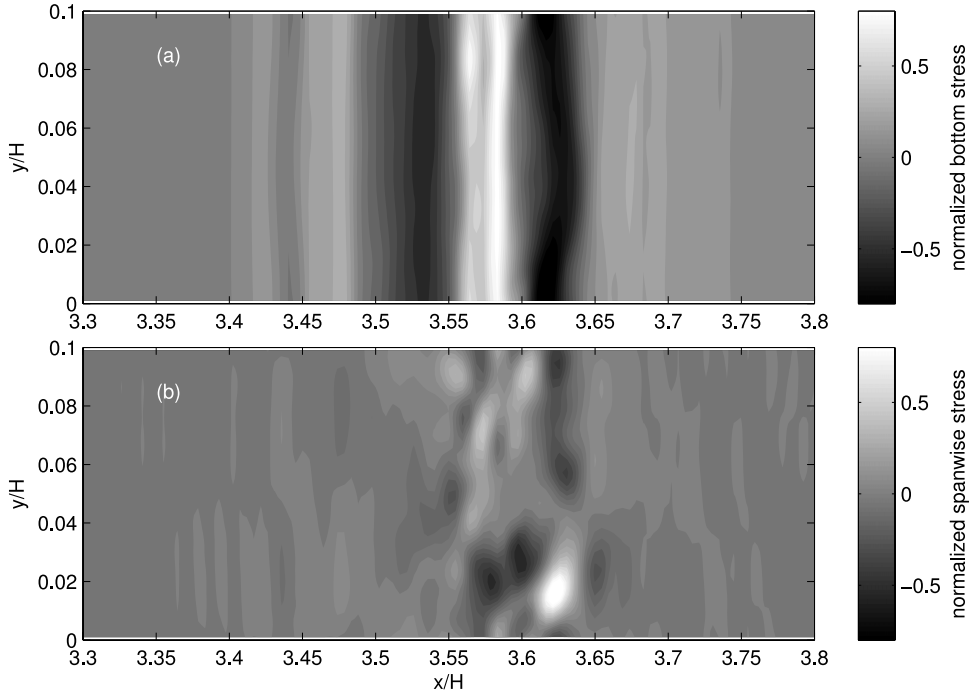

FIG. 7. Shear stress for simulation 3DL1 at time $t = 6.44t^*$. (a) Bottom shear stress defined in (4), scaled by its maximum absolute value. (b) The spanwise shear stress, μv_z, also scaled by its maximum absolute value. At this time, the maximum bottom shear stress is about 3.6 times larger than the maximum spanwise shear stress.

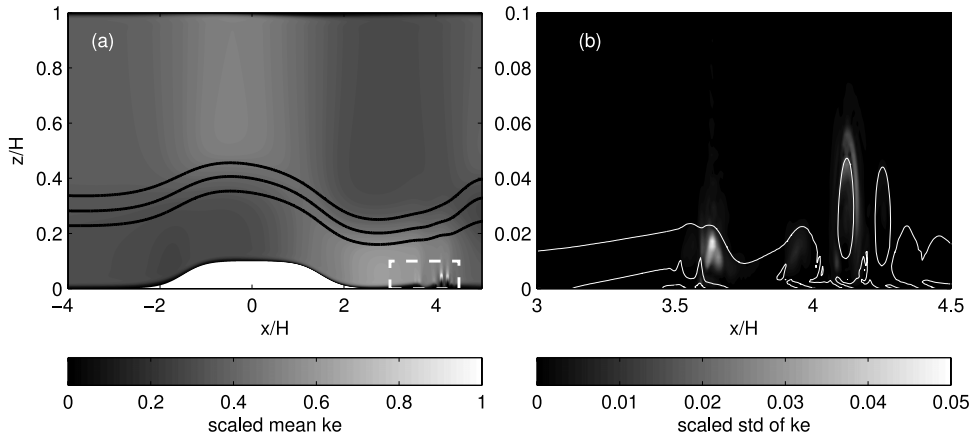

FIG. 8. As in Figure 6 but for 3DL2. The maximum pointwise kinetic energy at this time was 0.16 $m^2\ s^{-2}$.

Next, the Reynolds number is further reduced by a factor of two in simulation 3DL3 and the results are displayed Figure 9. Here, changes in the three-dimensional structure are apparent. First, the distribution of high kinetic energy in Figure 9(a) has changed. While high kinetic energy still occurs in the area of the instabilities, the scale is roughly the same as the kinetic energy induced by the topographic flow in the downstream accelerated region. This is qualitatively different from the previous cases where the kinetic energy induced by the instabilities is much stronger than in the other regions of the flow environment. Additionally, the three-dimensional structure has been very much reduced, as indicated in Figure 9(b). Note that the colour bar has been rescaled so that the maximum departures in this plot are less than 0.2% of the maximum kinetic energy, more than an order of magnitude less than that observed in case 3DL1. Additionally, the maximum departures occur in the second instability, i.e., the instability that is higher up into the water column. It is not surprising that the decrease in Reynolds number reduces the propensity for three-dimensional motions since the higher viscosity tends to damp all motion. However, the fact that the Reynolds number has only been decreased by a factor of four, or indeed a factor of two between the latter two cases, and still such different results are observed is interesting. These results suggest that it is important to use a Reynolds number that is within a factor of two or so of that representative of the flow environment if such instabilities are to be studied in great detail. Often numerical simulations and laboratory simulations utilize a Reynolds number lower than that representative of the geophysical scales of interest.

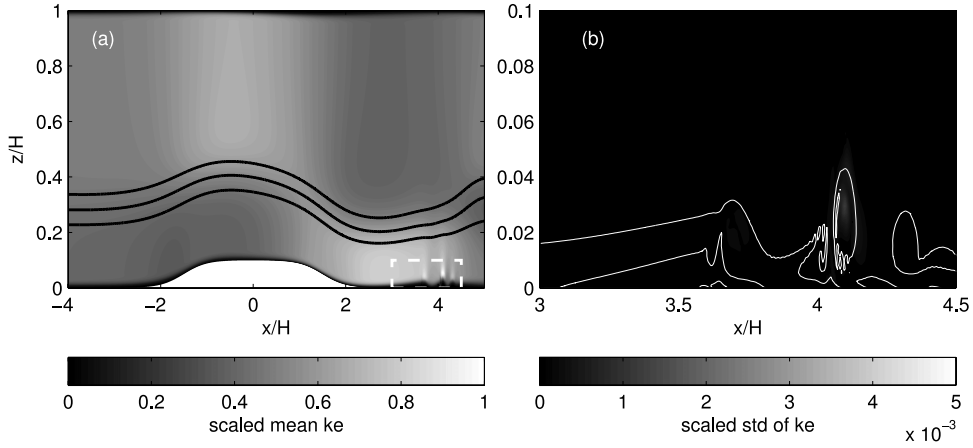

FIG. 9. As in Figure 6 but for 3DL3. The maximum pointwise kinetic energy at this time was 0.12 $m^2\ s^{-2}$.

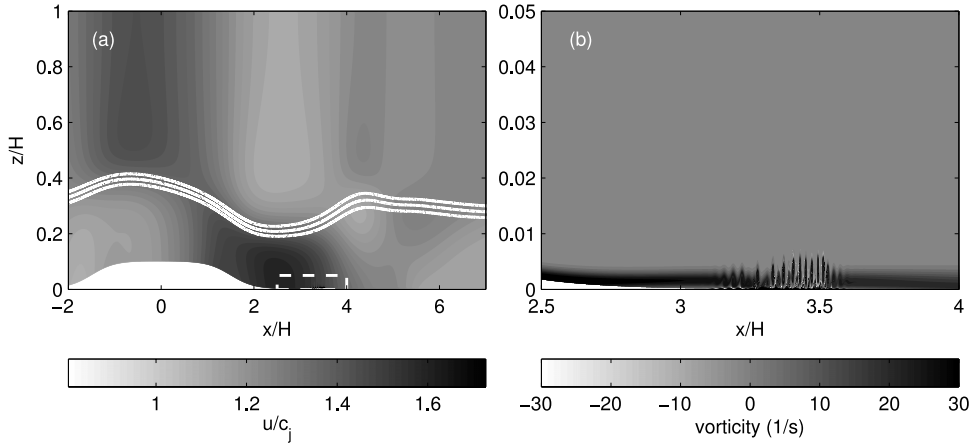

FIG. 10. Results from simulation 2DF1 at $t = 4.28t^*$. (a) Shaded contours of the streamwise velocity overlaid with three white density contours. (b) Shaded contours of the vorticity in the region of the white dashed rectangle from (a).

B. Field scale simulations

Many of the studies regarding the interaction of internal waves with the bottom boundary layer have examined laboratory scale experiments or numerical simulations. It is important to consider this interaction at field scales if sediment transport is an application of interest. As such, we have included an additional simulation with depth 10 m in Figure 10. The parameters for this simulation (2DF1) are outlined in Table II. Note that the Reynolds number has increased by an order of magnitude due to the use of the domain depth H as a typical length scale. The viscosity is the same as that used in simulation 2DL1 ($\nu = 10^{-6}$ m^2 s^{-1}) and the background current is of a similar magnitude.

The situation is very similar to that described in simulation 2DL1; a large wave has formed over the topography and large wave-induced velocities are found in the topographic lee in Figure 10(a). A series of instabilities develop in the boundary layer downstream of the topography, shown in detail in Figure 10(b). Since the ratio of the boundary layer thickness to the distance from the pycnocline has decreased, the instabilities do not interact with the pycnocline in this case. However, their role in transporting sediment laterally may be of interest in some applications.

This scaled-up case also exhibits strong departures in the bottom shear stress as demonstrated in Figure 11(a). The instabilities develop rather quickly producing high values of bottom shear stress covering a large area. A case with reduced Reynolds number by an order of magnitude to $Re = 5.5 \times 10^5$, labelled 2DF2, suggests a much different evolution of the boundary layer instabilities. First, the wavelength of the instabilities is much longer and they develop over a longer time frame, resulting in a more coherent and organized spatial pattern. Yet, even with the lower Reynolds number, the stress departure can reach very large values, although the number of peaks is smaller

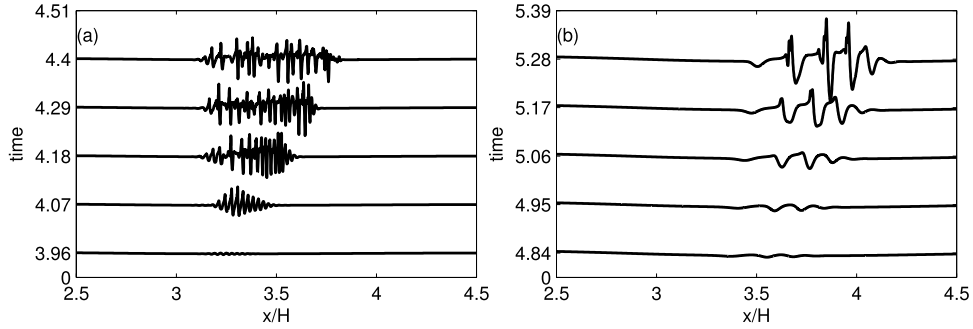

FIG. 11. The departure of the bottom shear stress from its upstream value for simulation (a) 2DF1 and (b) 2DF2. The maximum stress reached up to 38 times the upstream value in 2DF1 and 19 times the upstream value in 2DF2.

than the higher Reynolds number case. This suggests that an appropriate treatment of the viscous bottom boundary layer, in particular, the use of physical values of the viscosity, is essential for representing the behaviour of the bottom shear stress. The wave properties are not significantly altered by an order of magnitude increase in the viscosity, but their interaction with the bottom boundary is. These simulations both employed the same vertical and horizontal resolution.

The field scale simulations bring into question the appropriate definition of the Reynolds number in these flow environments. Motivated by previous studies on internal wave and boundary layer interaction,[4,10] we have chosen a Reynolds number based on the speed of the background current, the depth of the domain, and the kinematic viscosity, however, this choice results in an order of magnitude increase in the Reynolds just by changing the depth of the domain, even though the other flow properties such as the background current and viscosity are similar. This large change in Reynolds number does not reflect the nature of the instabilities at field scale and lab scale. In both cases, the instabilities have a characteristic vertical length scale on the order of 5-10 cm, as displayed in the vorticity contours of Figures 1 and 10 in the lab scale and field scale, respectively. This length scale, or the thickness of the bottom boundary layer (approximately 2 cm), may be a more representative choice for a Reynolds number based classification of the flow regime. These choices would lead to $Re \approx O(1 \times 10^4)$ in both cases 2DL1 and 2DF1, which more accurately reflects their similar characteristics in both the wave field and the boundary layer. A Reynolds number based on the momentum thickness of the boundary layer[12] gives $Re_{\theta_{sep}} \approx O(1 \times 10^3)$ in each case. These Reynolds number definitions have the disadvantage that they are difficult to prescribe prior to the commencement of the simulation and they may change in time as the boundary layer evolves, however, formulae to relate the momentum thickness to the large scale flow features exist.[12] Further, based on the boundary layer thickness one could formulate a Reynolds number criterion for the onset of three-dimensionalization. Although more cases should be used to evaluate this criterion in a future study, a simple comparison between the three lab scale simulations with changes in viscosity (3DL1, 3DL2, 3DL3) at $t \approx 5.3t^*$ would yield momentum thickness Reynolds numbers approximately 640, 305, and 115, respectively, suggesting a momentum thickness Reynolds number greater than 115 for the onset of three-dimensionalization. This Reynolds number calculation is more applicable in scaling from lab to field scales.

This point is emphasized further by comparing changes in the Reynolds number at both field and lab scales in Figure 12 where we plot the streamwise velocity field for four simulations. First, two lab scale simulations 2DL1 with $Re = 3.5 \times 10^5$ and 2DL2 with $Re = 3.5 \times 10^6$ are shown in panels (a) and (d), respectively. Between these two cases, the Reynolds number has increased by an order of magnitude because the viscosity was decreased from 10^{-6} m^2 s^{-1} to 10^{-7} m^2 s^{-1}. Note

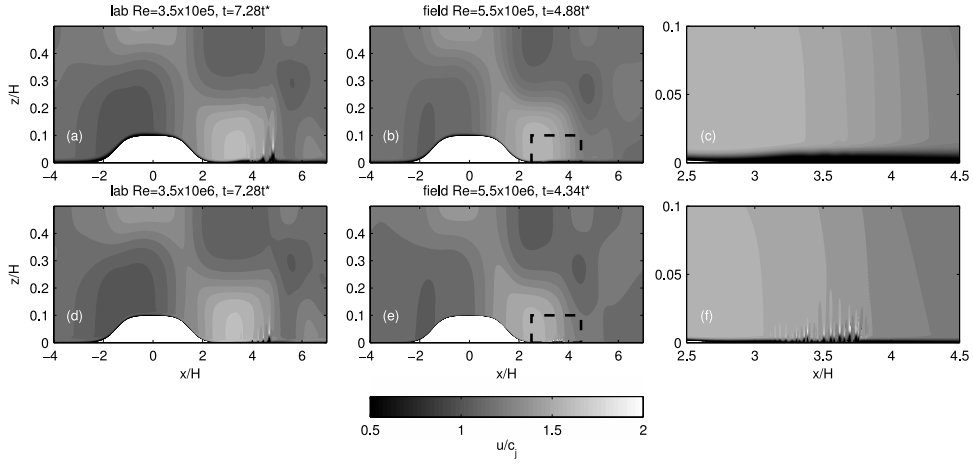

FIG. 12. Streamwise velocity field comparisons at different Reynolds numbers and scales. (a) Simulation 2DL1 with $Re = 3.5 \times 10^5$ at $t = 7.28t^*$. (b) Simulation 2DF2 with $Re = 5.5 \times 10^5$ at $t = 4.88t^*$. (c) A zoom in of the dashed rectangle in panel (b). (d) Simulation 2DL2 with $Re = 3.5 \times 10^6$ at $t = 7.28t^*$. (e) Simulation 2DF1 with $Re = 5.55 \times 10^6$ at $t = 4.34t^*$. (f) Zoom in of the dashed rectangle in panel (e).

that it was necessary to increase the number of vertical grid points by a factor of two in order to resolve the boundary layer in the lower viscosity case. Both plots are at $t = 7.28t^*$. The instabilities are very similar between the two cases and they form at approximately the same time. By contrast, similar Reynolds numbers at the field scale lead to a very different comparison. In panels (b) and (c), the streamwise velocity for simulation 2DF2 with $Re = 5.5 \times 10^5$ is shown at $t = 4.88t^*$. Panels (e) and (f) show the streamwise velocity for simulation 2DF1 with $Re = 5.5 \times 10^6$ at $t = 4.34t^*$. In these two cases, the viscosity was decreased from 10^{-5} m^2 s^{-1} to 10^{-6} m^2 s^{-1}. The boundary layer structure between these two cases is very different. Even though the lower Reynolds number simulation is shown at a later time, instabilities are only starting to form. In the high Reynolds number case, the instabilities are well-developed. An order of magnitude increase in the Reynolds number leads to a very different change in the boundary layer dynamics at lab and field scales, suggesting that the Reynolds number has not been formulated correctly and supporting an alternate definition as suggested above. The momentum thickness Reynolds number[12] calculated at the times shown in Figure 12 yields $Re_{\theta_{sep}} = 502$ for panel (a), $Re_{\theta_{sep}} = 650$ for panel (b), $Re_{\theta_{sep}} = 1800$ for panel (d), and $Re_{\theta_{sep}} = 1900$ for panel (e).

Finally, a high resolution three-dimensional version of 2DF1 was performed by extending a two-dimensional output into the spanwise dimension with white noise of scale 0.01. The spanwise extent is 10 cm with 96 grid points, giving a spanwise grid spacing $\Delta y \approx 0.001$ m. Note that the spanwise length is the same as that at the lab scale. This choice is justified because the streamwise and vertical size of the instabilities (about 25 cm by 5 cm) does not change significantly between the lab and field cases. The three-dimensional simulation was commenced at $t = 4.1t^*$ at which point an array of instabilities are found in the boundary layer but have not yet undergone any significant break down. Three-dimensional features of this experiment are presented in Figure 13 from $t = 4.15t^*$ at which point the simulation was terminated due to the extensive computational requirements.

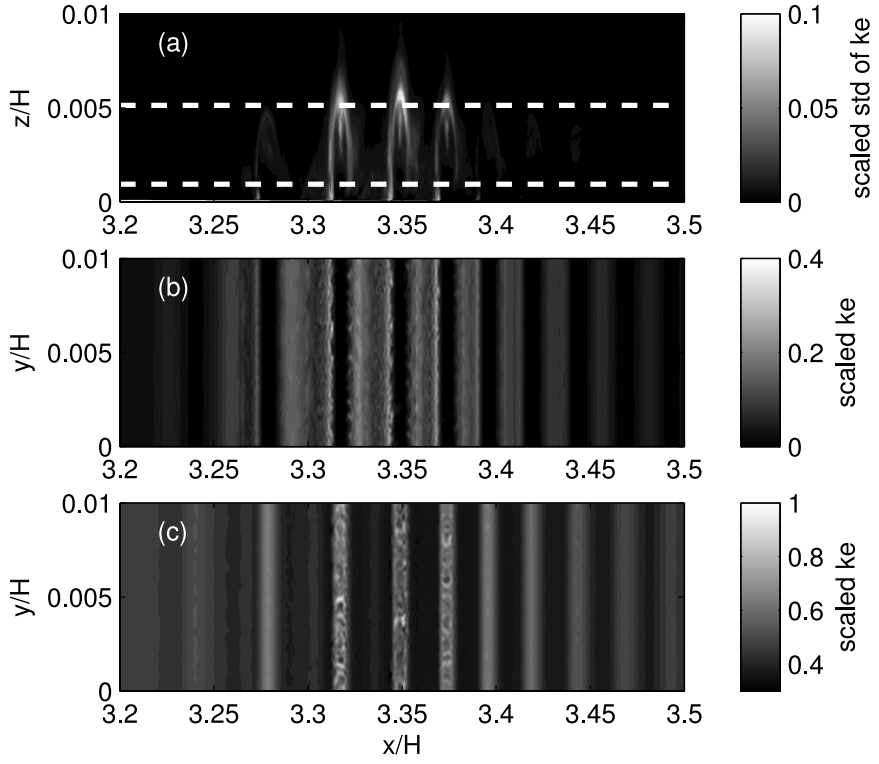

FIG. 13. Results from simulation 3DF1 at $t = 4.15t^*$. (a) Spanwise standard deviation of the kinetic energy scaled by the pointwise maximum of the kinetic energy. Horizontal slices of the kinetic energy scaled by the pointwise maximum of kinetic energy at (b) $z = 0.001H$ and (c) $z = 0.005H$. The dashed white lines in panel (a) indicate the height of these horizontal surfaces.

In the vicinity of the instabilities, the flow field three-dimensionalizes quickly. At this time, the spanwise standard deviation of the kinetic energy has reached up to 10% of the pointwise maximum kinetic energy as seen in a set of three boundary layer instabilities shown in Figure 13(a). Each instability exhibits a perimeter of strong three-dimensionalization surrounding a dark separation region in the centre. The structure looks different than that seen in the lab scale simulations where three-dimensional structure appears less organized perhaps because they were allowed to three-dimensionalize over a longer period of time. Another explanation could be that the spanwise dimension has not been scaled up and the flow is too confined in that dimension. Some of the largest standard deviations occur at the upper edge of each instability, through $z \approx 0.005H$. High values are also seen very close to bottom boundary through $z \approx 0.001H$, just upstream of the separation bubble associated with each instability. The three-dimensional structure at these two heights is shown in horizontal cross-sections of the kinetic energy scaled by its pointwise maximum in Figures 13(b) at $z = 0.001H$ and 13(c) at $z = 0.005H$. Close to the bottom boundary, the three-dimensional structure around the dark separation regions is apparent in Figure 13(b), possibly indicating a region associated with the onset of three-dimensional break down had the simulation been carried out for longer. At $z = 0.005H$, some three-dimensional structure is observed along three bands associated with the upper regions of the three largest instabilities.

In addition, the bottom shear stress and spanwise shear stress both contain significant spanwise structure at this time (Figure 14). The areas of large spanwise variation are aligned between both fields, and are also aligned with areas of three-dimensional structure in the kinetic energy (Figure 13). The largest deviations in the bottom shear stress occur along the streamwise direction, but small changes occur along the spanwise. The maximum absolute value of the bottom shear stress is about four times larger than the maximum absolute value of the spanwise shear stress. While the bottom shear stress is the larger contributor to high stress values, the spanwise shear stress imposes significant variations in the spanwise dimension. This is a similar finding to what was seen at lab scales.

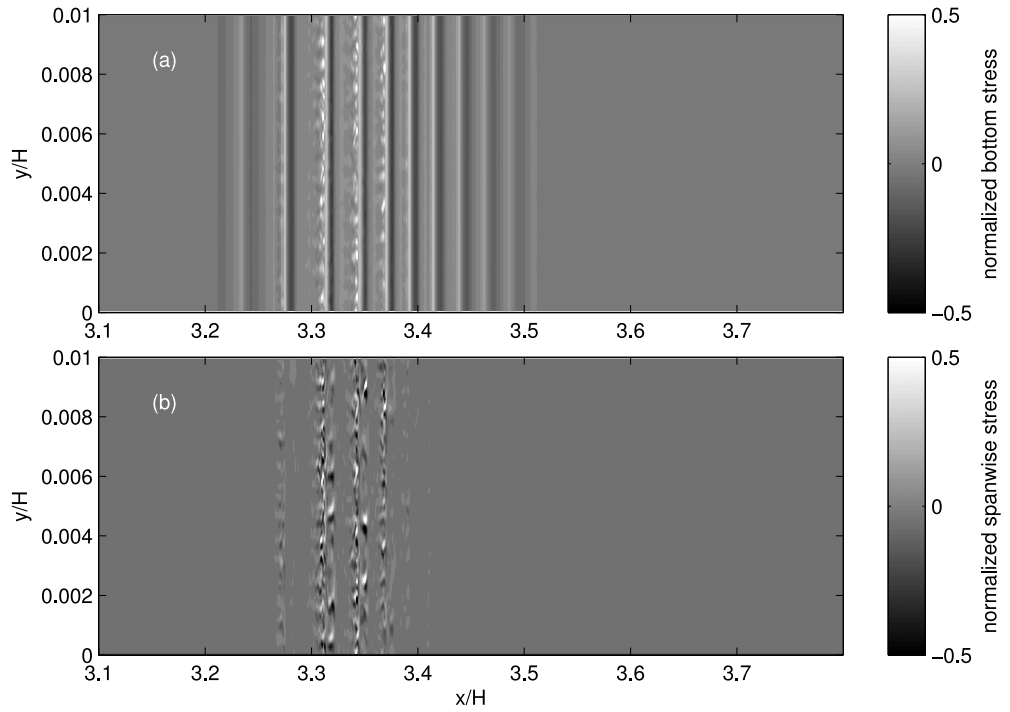

FIG. 14. Shear stress for simulation 3DF1 at time $t = 4.15t^*$. (a) Bottom shear stress defined in (4), scaled by its maximum absolute value. (b) The spanwise shear stress, μv_z, also scaled by its maximum absolute value. At this time, the maximum bottom stress is about 3.9 times larger than the maximum spanwise shear stress.

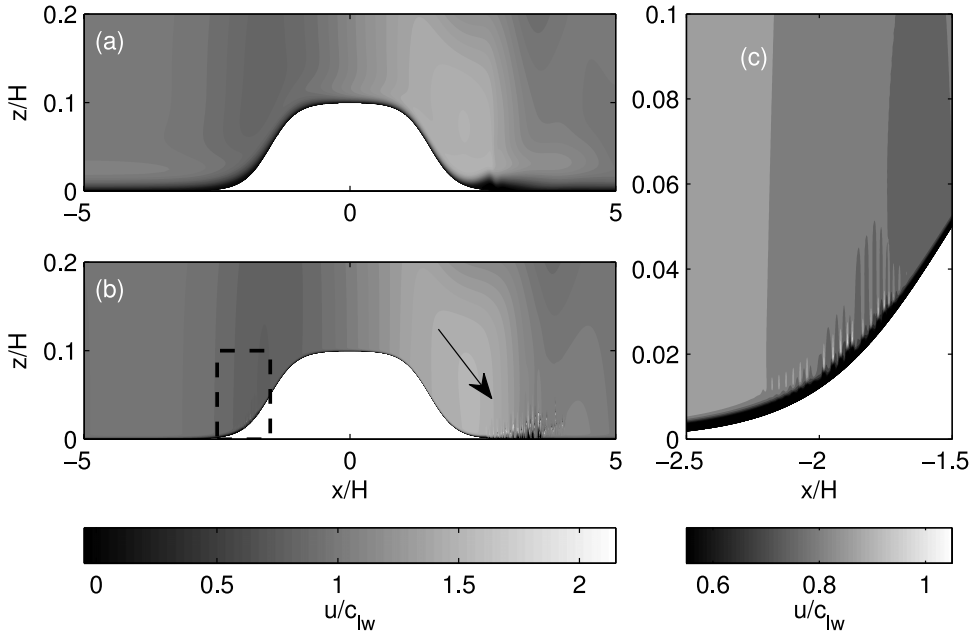

FIG. 15. Horizontal velocity field scaled by the linear long wave speed c_{lw} from two subcritical cases at $t \approx 5.3t^*$. (a) Lab scale simulation 2DLS. (b) Field scale simulation 2DFS. (c) A close up of the black dashed rectangle in (b).

C. Subcritical cases

Results from two additional subcritical simulations, one at laboratory scale and one at field scale, are provided in Figure 15. Both of these simulations have a background speed $U_0 = 1.05c_{lw}$. Although the background current is larger than the linear long wave speed, it is still smaller than the conjugate slow speed c_j in both cases, and so formally subcritical. As such, upstream propagating disturbances could be expected after long enough simulation times. Additionally, the domain of the lab scale case has been extended to 28 m in order to prevent wraparound effects. The grid spacing is kept the same.

The horizontal velocity field at $t \approx 5.3t^*$ is plotted for the laboratory scale case in panel (a) and the field scale case in panel (b). Recall that the time scale t^* is an advective time scale based on the wave propagation speed, meaning that the wave-induced currents are in a similar position relative to the topography in both the laboratory scale and field scale cases. Both figures display a wave with large velocities of approximately the same scale relative to the linear long wave speed on the lee side of the topography. However, the advective time scale is much larger in the field scale, so this simulation extends longer into physical time than the laboratory scale simulation (120 s in field scale versus 20 s in laboratory scale). As such, the instabilities downstream of the topography are much more developed in the field scale simulation. Additionally, Figure 15(c) shows a set of instabilities beginning to form on the upstream slope in the field scale case. The lab scale simulation does not exhibit any upstream instabilities at this time, but they are well established later, at $t = 14t^*$, in addition to a significant break down of the downstream instabilities (not shown). There is a clear separation of time and length scales between the instabilities and the internal wave responsible for their generation. Although the currents induced by the internal waves are responsible for the generation of these instabilities, the amount of time that these currents spend interacting with the bottom boundary is an important factor in determining where and when these instabilities develop, which can lead to different behaviours at field and lab scales. Although it is common to non-dimensionalize when comparing between scales, the time span of the current-boundary layer interaction is also important to consider. Note that the boundary layer appears thicker in the lab scale simulation, but the vertical and horizontal dimensions have been scaled by the domain depth H which is a factor of 10 larger in the field scale, so the boundary layers are approximately the same height.

IV. DISCUSSION AND CONCLUSIONS

This study has produced numerical simulations of internal wave generation over isolated topography and their interaction with a viscous bottom boundary layer. Simulations at laboratory scales of 1 m depth and larger scales of 10 m depth have been considered, both resulting in the production of boundary layer instabilities in the lee of an elevated topography when the pycnocline is placed below the mid-depth. Differences in elevation and depression topography have been highlighted, but both considering supercritical flows for which the background current speed is greater than the conjugate flow speed. Over depression topography, instabilities form in a separation region on the upstream slope of the topography. It is suggested that the presence of the viscous boundary layer and the separation region can significantly alter the generation of an internal wave found over the topography, reducing the wave amplitude when compared to what would be predicted by a steady-state inviscid theory in the case of near-critical flows. Future work will examine whether or not the pressure gradient is modified enough to preclude the formation of large trapped waves of depression at field scales. Over elevated topography, accelerated flow over the downstream slope leads to a convergence zone and the generation of boundary layer instabilities in the topographic lee. As such, the internal wave over the elevated topography is not greatly altered from its inviscid counterpart, at least in the case of the supercritical flows considered here. Comparisons between elevation and depression topographies were motivated by previous inviscid studies that found much larger amplitude trapped internal waves over depression topography.[15]

The bottom shear stress was examined for the instabilities near both the elevation and depression topography where large departures from the upstream values were found in both cases. However, the onset of large stress values occurs more quickly in the elevation case and covers a larger proportion of the domain. Additionally, in the elevation case and after long integration times, instabilities can form over the upstream topographic slope and are advected downstream, which may be of consequence to sediment transport over ridges. These results suggest that supercritical flow over elevated topography may affect sediment distribution over a larger geographical area than supercritical flow over depression topography.

A set of three-dimensional simulations over elevated topography has been analyzed to determine the effect of viscosity on the three-dimensionalization of these instabilities. Three-dimensional characteristics were quantified by examining the spanwise standard deviation and mean of the kinetic energy, scaled by the pointwise maximum of the kinetic energy. It is found that minor changes in the viscosity, for example, an increase by a factor of four, can significantly alter the onset and strength of three-dimensionalization. This is an important consideration for simulations that employ an overly diffusive boundary layer parametrization, particularly in the setting of three-dimensional simulations which have a very high demand for computing resources. Other work has shown that two-dimensional simulations of separation bubbles over airfoils do not adequately represent the three-dimensional bursting motions.[23] Simulations of shoaling internal waves found major differences in the amount of dissipation and mixing when comparing between two and three dimensions.[25] As such, simulations examining sediment resuspension due to vortex shedding should carefully parametrize the effects of viscosity, as the three-dimensional nature of these instabilities has been shown to be sensitive to this parameter.

Laboratory scale simulations of 1-m depth with elevated topography have been extended to larger scales with a depth of 10 m. Boundary layer instabilities form in the lee of the elevated topography under the same mechanisms as those simulations at lab scales. It was noted that extensions to field scale should not use a Reynolds number length scale based on the depth of the domain as has been suggested by some of the literature.[4,10] A length scale that measures the boundary layer thickness, for example, the momentum thickness Reynolds number suggested by Aghsaee *et al.*,[12] is more appropriate and reflects the similarities between lab and field scales. In particular, the streamwise and spanwise extent of the instabilities is similar at both field and lab scales, given the similar values of the background current and viscosity.

Finally, two formally subcritical simulations at both lab scale and field scale have been performed with background currents $U_0 = 1.05c_{lw}$ but $U_0 < c_j$. These simulations demonstrated a clear separation of time scales between the onset of the instabilities and the advection of the wave.

Although the location of the wave relative to the topography was similar in each case, the large currents induced by the wave at field scale acted on the bottom boundary layer over a longer period of time and so the instabilities were more developed.

Further work examining the generation and evolution of these instabilities at field scales is warranted. In particular, an evaluation of vortex shedding criteria at field scales with comparisons to lab scales would advance our understanding of how these processes scale up and, hence, their impact on sediment transport and resuspension in real world applications. Many observational studies suggest a link between internal wave propagation and increased sediment concentrations.[1,5,18,32] Numerical simulations and laboratory experiments enable a systematic investigation of the parameter regimes associated with these processes.

While the parameter space available is very large, and three dimensional simulations cannot span more than a select few points within it, our study has several important conclusions that have not been addressed in the literature to date. We rank these conclusions in order of importance, as we see it. First, our study suggests that at experimental scales, wave generation over broad depression topography is affected by viscosity in a much more dramatic manner than corresponding elevation topography, including a nearly complete absence of large waves. Second, the bottom boundary layer instability and its three-dimensionalization is strongly affected by increases in the numerical viscosity. This suggests that numerical methodology that treats the near bottom region in a different manner from the wave body may be essential to pushing the Reynolds number to ocean relevant values. Third, we have identified a novel instability over the upstream slope of elevation topography which occurs due to the opposing effects of topography slope and wave-induced currents.

ACKNOWLEDGMENTS

This work was supported by the Natural Sciences and Engineering Research Council of Canada. We would like to thank two anonymous reviewers for their detailed comments and suggestions which greatly improved the manuscript.

[1] D. Bogucki, T. Dickey, and L. Redekopp, "Sediment resuspension and mixing by resonantly generated internal solitary waves," J. Phys. Oceanogr. **27**(7), 1181–1196 (1997).
[2] K. Helfrich and W. Melville, "Long nonlinear internal waves," Annu. Rev. Fluid Mech. **38**, 395 (2006).
[3] M. Stastna and K. Lamb, "Vortex shedding and sediment resuspension associated with the interaction of an internal solitary wave and the bottom boundary layer," Geophys. Res. Lett. **29**(11), 7-1–7-3, doi:10.1029/2001GL014070 (2002).
[4] P. Diamessis and L. Redekopp, "Numerical investigation of solitary internal wave-induced global instability in shallow water benthic boundary layers," J. Phys. Oceanogr. **36**(5), 784 (2006).
[5] D. Bogucki and L. Redekopp, "A mechanism for sediment resuspension by internal solitary waves," Geophys. Res. Lett. **26**(9), 1317–1320, doi:10.1029/1999GL900234 (1999).
[6] J. Olsthoorn and M. Stastna, "Numerical investigation of internal wave-induced sediment motion: Resuspension versus entrainment," Geophys. Res. Lett. **41**(8), 2876–2882, doi:10.1002/2014GL059826 (2014).
[7] M. Stastna and K. Lamb, "Sediment resuspension mechanisms associated with internal waves in coastal waters," J. Geophys. Res.: Oceans **113**(C10), C10016, doi:10.1029/2007JC004711 (2008).
[8] L. S. Quaresma, J. Vitorino, A. Oliveira, and J. da Silva, "Evidence of sediment resuspension by nonlinear internal waves on the western Portuguese mid-shelf," Mar. Geol. **246**(2), 123–143 (2007).
[9] P. Aghsaee and L. Boegman, "Experimental investigation of sediment resuspension beneath internal solitary waves of depression," J. Geophys. Res.: Oceans **120**, 3301, doi:10.1002/2014jc010401 (2015).
[10] M. Carr, P. Davies, and P. Shivaram, "Experimental evidence of internal solitary wave-induced global instability in shallow water benthic boundary layers," Phys. Fluids **20**, 066603 (2008).
[11] M. Dunphy, C. Subich, and M. Stastna, "Spectral methods for internal waves: Indistinguishable density profiles and double-humped solitary waves," Nonlinear Processes Geophys. **18**(3), 351–358 (2011).
[12] P. Aghsaee, L. Boegman, P. Diamessis, and K. Lamb, "Boundary-layer-separation-driven vortex shedding beneath internal solitary waves of depression," J. Fluid Mech. **690**, 321 (2012).
[13] P. Baines, *Topographic Effects in Stratified Flows* (Cambridge University Press, 1995).
[14] M. Stastna, "Resonant generation of internal waves by short length scale topography," Phys. Fluids **23**(11), 116601 (2011).
[15] N. Soontiens, M. Stastna, and M. Waite, "Trapped internal waves over topography: Non-boussinesq effects, symmetry breaking and downstream recovery jumps," Phys. Fluids **25**, 066602 (2013).
[16] R. Grimshaw and N. Smyth, "Resonant flow of a stratified fluid over topography," J. Fluid Mech. **169**, 429 (1986).
[17] M. Carr, M. Stastna, and P. Davies, "Internal solitary wave-induced flow over a corrugated bed," Ocean Dyn. **60**(4), 1007–1025 (2010).
[18] D. R. Johnson, A. Weidemann, and W. S. Pegau, "Internal tidal bores and bottom nepheloid layers," Cont. Shelf Res. **21**(13), 1473–1484 (2001).

[19] J. M. Klymak and J. N. Moum, "Internal solitary waves of elevation advancing on a shoaling shelf," Geophys. Res. Lett. **30**(20), 3-1–3-4, doi:10.1029/2003GL017706 (2003).
[20] L. Boegman and G. N. Ivey, "Flow separation and resuspension beneath shoaling nonlinear internal waves," J. Geophys. Res.: Oceans **114**(C2), C02018, doi:10.1029/2007jc004411 (2009).
[21] D. Bourgault, M. Morsilli, C. Richards, U. Neumeier, and D. E. Kelley, "Sediment resuspension and nepheloid layers induced by long internal solitary waves shoaling orthogonally on uniform slopes," Cont. Shelf Res. **72**, 21–33 (2014).
[22] O. M. Cheriton, E. E. McPhee-Shaw, W. J. Shaw, T. P. Stanton, J. G. Bellingham, and C. D. Storlazzi, "Suspended particulate layers and internal waves over the southern monterey bay continental shelf: An important control on shelf mud belts?," J. Geophys. Res.: Oceans **119**(1), 428–444, doi:10.1002/2013JC009360 (2014).
[23] M. Alam and N. Sandham, "Direct numerical simulation of short laminar separation bubbles with turbulent reattachment," J. Fluid Mech. **410**(1), 1–28 (2000).
[24] S. Harnanan, N. Soontiens, and M. Stastna, "Internal wave boundary layer interaction: A novel instability over broad topography," Phys. Fluids **27**(1), 016605 (2015).
[25] R. S. Arthur and O. B. Fringer, "The dynamics of breaking internal solitary waves on slopes," J. Fluid Mech. **761**, 360–398 (2014).
[26] B. Boehrer and M. Schultze, "Stratification of lakes," Rev. Geophys. **46**(2), RG2005, doi:10.1029/2006RG000210 (2008).
[27] K. Lamb and B. Wan, "Conjugate flows and flat solitary waves for a continuously stratified fluid," Phys. Fluids **10**(8), 2061 (1998).
[28] N. Soontiens, C. Subich, and M. Stastna, "Numerical simulation of supercritical trapped internal waves over topography," Phys. Fluids **22**(11), 116605 (2010).
[29] C. Subich, K. Lamb, and M. Stastna, "Simulation of the Navier-Stokes equations in three dimensions with a spectral collocation method," Int. J. Numer. Methods Fluids **73**, 103–129 (2013).
[30] C. Loken, D. Gruner, L. Groer, R. Peltier, N. Bunn, M. Craig, T. Henriques, J. Dempsey, C. Yu, J. Chen *et al.*, "Scinet: Lessons learned from building a power-efficient top-20 system and data centre," J. Phys.: Conf. Ser. **256**, 012026 (2010).
[31] P. Kundu and I. Cohen, *Fluid Mechanics* (Elsevier Academic Press, 2008).
[32] D. J. Bogucki, L. Redekopp, and J. Barth, "Internal solitary waves in the coastal mixing and optics 1996 experiment: Multimodal structure and resuspension," J. Geophys. Res.: Oceans **110**(C2), C02024, doi:10.1029/2003jc002253 (2005).